

Fractional matter coupled to the emergent gauge field in a quantum spin ice

Victor Porée^{1†}, Han Yan,^{2†} Félix Desrochers,^{3†} Sylvain Petit^{4‡}, Elsa Lhotel^{5‡}, Markus Appel⁶, Jacques Ollivier⁶,
Yong Baek Kim,³ Andriy H. Nevidomskyy² & Romain Sibille^{1*}

¹Laboratory for Neutron Scattering and Imaging, Paul Scherrer Institut, 5232 Villigen PSI, Switzerland, ²Department of Physics & Astronomy, Rice University; Houston, TX 77005, USA, ³Department of Physics, University of Toronto, Toronto, Ontario M5S 1A7, Canada, ⁴LLB, CEA, CNRS, Université Paris-Saclay, CEA Saclay, 91191 Gif-sur-Yvette, France, ⁵Institut Néel, CNRS – Université Grenoble Alpes, 38042 Grenoble, France, ⁶Institut Laue-Langevin, CS 20156, F-38042 Grenoble Cedex 9, France, *email: romain.sibille@psi.ch †These authors contributed equally to this work. ‡These authors contributed equally to this work.

Electronic spins can form long-range entangled phases of condensed matter named quantum spin liquids^{1–4}. Their existence is conceptualized in models of two- or three-dimensional frustrated magnets that evade symmetry-breaking order down to zero temperature. Quantum spin ice (QSI) is a theoretically well-established example described by an emergent quantum electrodynamics, with excitations behaving like photon and matter quasiparticles^{5–6}. The latter are fractionally charged and equivalent to the ‘spinons’ emerging from coherent phases of singlets in one dimension, where clear experimental proofs of fractionalization exist^{7–9}. However, in frustrated magnets it remains difficult to establish consensual evidence for quantum spin liquid ground states and their fractional excitations. Here, we use backscattering neutron spectroscopy¹⁰ to achieve extremely high resolution of the time-dependent magnetic response of the candidate QSI material $\text{Ce}_2\text{Sn}_2\text{O}_7$ (refs. 11,12). We find a gapped spectrum featuring a threshold and peaks that match theories^{13–16} for pair production and propagation of fractional matter excitations (spinons) strongly coupled to a background gauge field. The observed peaks provide evidence for a QSI through spectroscopic signatures of space-time symmetry fractionalization, while the threshold behavior corroborates the regime of strong light-matter interaction predicted for the emergent universe in a QSI¹⁷.

The idea that certain phases of condensed matter have “quantum orders” alludes to the description of their electronic correlations with an effective low-energy gauge theory, without spontaneous symmetry breaking^{18–19}. The emergent gauge field reflects the long-range and/or topological entanglement of a complex ground-state wavefunction, which results in a variety of exotic properties such as excitations carrying fractional quantum numbers. A famed example is the collective behavior of a two-dimensional electron gas where electrons acquire

a fractional elementary charge²⁰. Similar states termed quantum spin liquids (QSL) are predicted to emerge in models of two- and three-dimensional frustrated magnets^{1–4}. Their effective low-energy description is a deconfined gauge theory where quasiparticles that carry spin 1/2 and no charge, known as spinons, can propagate coherently with the background gauge field. However, because the fractional spin excitations interact strongly with the background gauge field under which they are charged, their dynamics is highly non-trivial. The symmetries of the underlying crystal structure can additionally enrich topological phases: spinons can carry fractional crystal momentum, leading to enhanced periodicity of the excitation spectrum in momentum^{21–22}.

A prototypical model of a three-dimensional frustrated magnet is the spin ice²³, whose magnetic degrees of freedom reside on a lattice of corner-sharing tetrahedra where each motif results in a local ‘2-in-2-out’ constraint due to nearest-neighbor ferromagnetic interactions $J_{//}$. The classical limit of this model is called classical spin ice (CSI) and consists of a macroscopically degenerate manifold of ground states obeying this local rule reminiscent of the arrangement of hydrogens in water ice²⁴ (Fig. 1a). Such physics is realized in rare-earth pyrochlore materials with large uniaxial magnetic moments, where thermally-driven spin flips create pairs of emergent fractional quasiparticles called “magnetic monopoles” (Fig. 1b-c)²⁵. These quasiparticles interact through an effective Coulomb potential, which, in materials like $\text{Ho}_2\text{Ti}_2\text{O}_7$ (ref. 26), arises from classical dipole–dipole forces. It is theoretically well established that a true QSL can be stabilized in rare-earth pyrochlores with an isolated ground-state doublet (an effective spin-1/2) by nearest-neighbor transverse interactions J_{\perp} acting perturbatively on CSI states^{5–6,27–29}. The dominant tunneling process⁵ of this quantum spin ice (QSI) is a ring exchange term ($J_{ring} \sim J_{\perp}^3/J_{//}^2$) that corresponds to flipping loops of head-to-tail spins on a hexagonal plaquette⁵ (Fig. 1d). The ring exchange terms have local symmetry properties – a U(1) invariance – making their effective lattice gauge theory analogous to quantum electrodynamics (QED). The sign of the transverse interaction translates into distinct QSI phases where the hexagonal plaquettes are threaded by static 0 ($J_{\perp} > 0$) and π ($J_{\perp} < 0$) fluxes of the emergent gauge field^{30–31}. At temperatures $T \approx J_{ring}$, the QSI ground state is characterized by gapless, linearly dispersing excitations, which are transverse fluctuations of the gauge field and correspond to the photons of the emergent QED. At higher temperatures $J_{ring} \ll T \ll J_{//}$, however, thermal fluctuations destroy part of the quantum coherence and gradually restore a CSI^{27–28}. The exotic nature of QSI also stands out from its gapped, fractional excitations – spinons, which are characterized by a larger energy scale set by $J_{//}$. They correspond to “magnetic monopoles” (electric charges in QED language) executing coherent quantum motion^{5–6}.

Neutrons can create spin-flip excitations leading to integer changes of the total spin, which in a QSL is expected to generate pairs of spinons that separate and execute quantum motion under the constraints of the emergent background gauge field. Here, we present neutron spectroscopy data of a candidate QSI material – $\text{Ce}_2\text{Sn}_2\text{O}_7$ (refs. 11–12), providing a wavevector-integrated spectrum of its magnetic response with μeV resolution. From a technical perspective, our findings demonstrate an advance in terms of energy resolution improved by more than an order of magnitude compared to other studies, allowing quantitative comparisons with theories for spinon dynamics in QSI.

We first present inelastic neutron scattering (INS) data acquired using a time-of-flight (TOF) spectrometer (Fig. 2a), at different temperatures across the dominant energy scale in $\text{Ce}_2\text{Sn}_2\text{O}_7$ ($J_{JJ} \approx 50 \mu\text{eV} \approx 0.6 \text{ K}$)¹². The magnetic response is essentially inelastic, as shown by the lack of temperature dependence of the elastic line (Fig. 2c). We use the highest temperature spectrum measured at 5 K, which is well above the correlated regime in this material, in order to evaluate the magnetic scattering $S(E)$ at lower temperatures by difference. Fig. 2b shows the imaginary part of the dynamic spin susceptibility calculated as $\chi''(E) = S(E) \times [1 - \exp(-E/k_B T)]$, where E is the neutron energy transfer and k_B is the Boltzmann's constant. This data shows the typical magnetic response in cerium pyrochlores^{12,32–33}: a continuum of spin excitations, as expected from spinons, peaked at the energy of the dominant exchange interaction J_{JJ} . We fit these spectra using a phenomenological Lorentzian peak shape in order to capture their temperature evolution (Fig. 2d-f). The center of the band is temperature independent within the resolution of the measurement, and the intensity of the continuum increases while its width reduces upon cooling. This evolution occurs mostly below 1 K, which is consistent with changes previously reported in bulk magnetic susceptibility and diffuse magnetic scattering^{11–12}. At the lowest measured temperature $T \sim 0.2 \text{ K}$, the data suggest a gapped spectrum with a non-trivial density of states (DOS) as shown in the inset of Fig. 2b. The TOF energy resolution of about $11 \mu\text{eV}$, however, does not allow to characterize the DOS in sufficient details.

While in TOF data the energy resolution is largely determined by the value and spread of the incident neutron wavelength, in backscattering spectroscopy it is mainly limited by the properties of crystal analyzers (Fig. 3a)¹⁰. Fig. 3b presents data acquired using a typical backscattering geometry where the incident energy is varied by Doppler effect, covering a window of $\pm 30 \mu\text{eV}$ around the elastic line with a high resolution (HR) of $0.7 \mu\text{eV}$.

Remarkably, this allows to observe the gap expected for spinons in a QSI (Fig. 3b inset). We also performed another experiment on the same instrument but using a recently developed option of ‘backscattering and time-of-flight spectrometer’ (BATS)³⁴. The latter provides a larger energy window of $\pm 250 \mu\text{eV}$, covering the entire bandwidth of the continuum in $\text{Ce}_2\text{Sn}_2\text{O}_7$. The increase in energy range comes at the cost of a coarser resolution of $3.3 \mu\text{eV}$ in our data, which still provides a more than threefold improvement in resolution over the TOF data in Fig. 2, and allows to capture fine details throughout the entire continuum.

In Fig. 3c we show the dynamic spin susceptibility $\chi''(E)$ obtained from combined HR and BATS data. At the base temperature of these experiments ($T \approx 0.17 \text{ K}$), $\chi''(E)$ can be well fitted using three Gaussian peaks of unconstrained widths. The maximum of the spectrum is reproduced by the main Gaussian peak located around $50 \mu\text{eV}$, above which a gradual intensity decrease is observed, well accounted for by the two weaker Gaussian peaks around $100 \mu\text{eV}$ and $150 \mu\text{eV}$, resulting in an overall asymmetric spectrum. Comparing the total fitted curve with an extrapolation of the experimental data points shows that the latter deviates slightly from the former at the lowest energy transfers, suggesting a threshold behavior at the bottom edge of the gapped continuum. The threshold eventually leads to a slight shoulder around $25 \mu\text{eV}$ energy transfers, identified in both the residual of the fit and the derivative of the extrapolated data (see Fig. 3c). At a higher temperature close to the uncorrelated regime ($T \approx 0.8 \text{ K}$), $\chi''(E)$ shows much weaker inelastic scattering, in excellent agreement with the TOF data.

A continuous spectrum of excitations is usually taken as a hallmark of QSL states, but there can be alternative explanations for their existence, such as disorder³⁵. These continua are therefore less deterministic of fractional quasiparticles than, for instance, jumps in the electric conductance of a two-dimensional electron gas²⁰. However, using combinations of analytical and numerical methods applied to the case of QSI^{13–16,36}, theory has recently focused on studying the DOS in the two-monopole sector (spinons). Importantly, these predictions provide more specific features than just a continuum, highlighting the structure of the underlying gauge field theory.

We first consider analytical results for the quantum dynamics of spinons hopping on a CSI background¹³, which is relevant at finite temperatures $J_{ring} \ll T \ll J_{//}$. The spinon hopping is constrained by the flippable spins in the CSI background – a condition that makes its propagation deviate significantly from a free hopping model and results in the unique threshold and asymmetry in the wavevector-integrated DOS¹³. Remarkably, this model captures the gross features observed in the excitation spectrum of $\text{Ce}_2\text{Sn}_2\text{O}_7$ (solid blue line in Fig. 4a). The threshold and

asymmetry of the continuum are important experimental observations, since they reflect the effect of the background gauge field on the dynamics of the fractional quasiparticles¹³. These two features, as well as the spinon band being centered on the energy of the dominant exchange, were also observed in numerical calculations using exact diagonalization¹³ as well as in quantum Monte Carlo simulations³⁶. The fitted exchange parameters based on the analytical hopping model, $J_{//} = 48 \mu\text{eV}$ and $J_{\pm} = -5.2 \mu\text{eV}$, are in good agreement with previous estimates based on fits of bulk thermodynamic properties at the mean-field level¹². In the context of $\text{Ce}_2\text{Sn}_2\text{O}_7$, $J_{//}$ refers to the coupling between octupolar components of the pseudo-spins³⁷ – a possibility that was predicted by theory^{38–39} and later observed experimentally¹². The asymmetry observed in the data indicates $J_{\pm} < 0$, as confirmed by the fit, because flipping the sign of J_{\pm} in the spinon hopping model would otherwise invert the shape of the spectrum along the energy axis¹³. The data thus confirms¹² that $\text{Ce}_2\text{Sn}_2\text{O}_7$ stabilizes the π -flux phase of QSI – the symmetry enriched state occupying a large portion of the QSI phase space⁴⁰, as also argued in $\text{Ce}_2\text{Zr}_2\text{O}_7$ (refs. 41-42). In the π -flux phase, translational symmetry fractionalizes³⁰⁻³¹, so that the spinons acquire a finite Aharonov-Bohm phase after transporting them around any hexagonal plaquette, leading to an enhanced periodicity of the two-spinon density of states in the Brillouin zone¹⁵⁻¹⁶.

A widely used theoretical framework to study QSI is gauge mean-field theory – a parton construction where bosonic spinons hop on the parent diamond lattice (c.f. Fig. 1) while interacting with the emergent $U(1)$ gauge field^{43,30}. A recent extension of this theory allows for the classification of symmetry fractionalization¹⁵, predicting clear spectroscopic signatures for the π -flux phase¹⁶. The spinon dispersion is expected to be composed of two bands that are mostly flat, leading to three peaks in the two-spinon density of states, with energy separations proportional to $J_{\pm}/J_{//}$ and intensity ratios reproducing an overall asymmetric spectrum. We use these results^{15,16} to fit $\chi''(E)$ including a phenomenological line broadening accounting for finite spinon lifetime and thermal fluctuations (black curve in Fig. 4b), giving $J_{//} = 69 \mu\text{eV}$ and $J_{\pm} = -17 \mu\text{eV}$. Remarkably, this model provides an explanation for the scattering observed at $E > 80 \mu\text{eV}$ that is not accounted for by the spinon hopping model where gauge fluxes are thermally activated and incoherent ($J_{ring} \ll T \ll J_{//}$). Although the intensity of the second peak is overestimated by the gauge mean-field theory at zero temperature, the level of agreement is remarkable given the nature of this model, i.e. the qualitative observation of peaks in the data and reproducing their positions in energy is significant. At finite temperatures $T \approx J_{ring}$, when gauge fluxes just start to freeze and become coherent, we expect that thermal fluctuations renormalize the relative intensities of the three peaks. The exchange constants translate into

$J_{ring} = 12.4 \mu\text{eV}$, which indicates that our experiments at $T \approx 0.17 \text{ K} \approx 15 \mu\text{eV}$ were indeed performed in the intermediate temperature regime where quantum coherence is not completely destroyed by thermal fluctuations. The physical existence of a second peak in the two-spinon density of states, at approximately the same energy as in the gauge mean-field theory, is also confirmed by recent numerical results using exact diagonalization⁴⁴ (grey curve in Fig. 4b).

We next consider the theoretical DOS taking into account the QED effects of spinons (electric charges) propagating on a coherent QSI background (photons)¹⁴. In this case, the most significant consequence of the Coulomb interaction is an abrupt step-function onset of spinon production at small momenta, which is known as the Sommerfeld enhancement¹⁴. Additionally, a crucial nature of the non-relativistic emergent QED is the hierarchy of exchange parameters, leading to spinons propagating much faster than the photons. This effectively leads to a broadening of the threshold at larger momenta, because spinons start to emit diffuse Cerenkov radiation¹⁴. The corresponding analytical model applies in the long-wavelength limit and thus can only be compared with our data at the low-energy onset of the spinon band. Therefore, we fit the analytical QED model to our HR backscattering data as shown with the dashed red lines in Fig. 4. The exchange parameters obtained from the spinon hopping model¹³ (Fig. 4a) and gauge mean field theory^{15,16} (Fig. 4b) were converted to predefined parameters in the QED model – namely the ring exchange, spinon mass and speed of light. The fine-structure constant of the emergent QED – a dimensionless value characterizing how strongly light and matter couple, was fixed to $\alpha = 0.08$ based on numerical estimates for QSI¹⁷. After integrating the analytical model over the experimental window of momentum transfers, the calculated DOS matches the experiment remarkably well with a spinon gap $\Delta \approx 17 \mu\text{eV}$.

Finely resolving the spectrum of continuous excitations in a candidate QSI material opens the door to benchmarking important theory predictions on this unique quantum mechanical ground state. The agreement with the DOS expected for QSI is significant for several reasons. The characteristic features observed in the data – threshold, main peak and asymmetry, are signatures of the strong interaction of fractional spinons with the emergent gauge field. The asymmetry of the spectrum results from discernable peaks in the data, implying that the experiment probes a model-specific signature of fractionalization, at a temperature where quantum coherence has developed. This is especially remarkable given the notorious difficulties of experimentally assessing defining characteristics of QSLs. Moreover, we extract the exchange parameters of a QSL using a microscopic probe, directly from the spin liquid ground state excitation spectrum. This contrasts with the method of inferring exchange

parameters from spin waves of a related field-induced ordered phase. Finally, the comparison of the edge structure at the threshold of the spinon continuum appears to agree with predictions for the effects of photons on the pair production and propagation of electric charges. Recent numerical results have established how the emergent QED compares with that of our universe through estimates of its fine-structure constant¹⁷. It is predicted that the alternative vacuum of this condensed matter system is drastically different, with phenomena arising from strong light-matter interactions^{14,17}. Although our data cannot be used to directly determine the fine-structure constant, they corroborate these theoretical predictions. Momentum-resolved experiments on single-crystal samples would certainly further our understanding, however, directly fitting QED parameters from such data may require resolutions in both energy and momentum space that are far beyond current spectroscopic techniques. We note that a recent report possibly indicates the selection of a different ground state in samples of $\text{Ce}_2\text{Sn}_2\text{O}_7$ prepared hydrothermally and at much lower temperatures⁴⁵. Together with the fact that different ratios of exchange interactions were found in the three known cerium pyrochlore materials^{41-42,46}, this may suggest a high degree of tunability of the emergent QED, perhaps opening the door to its experimental control.

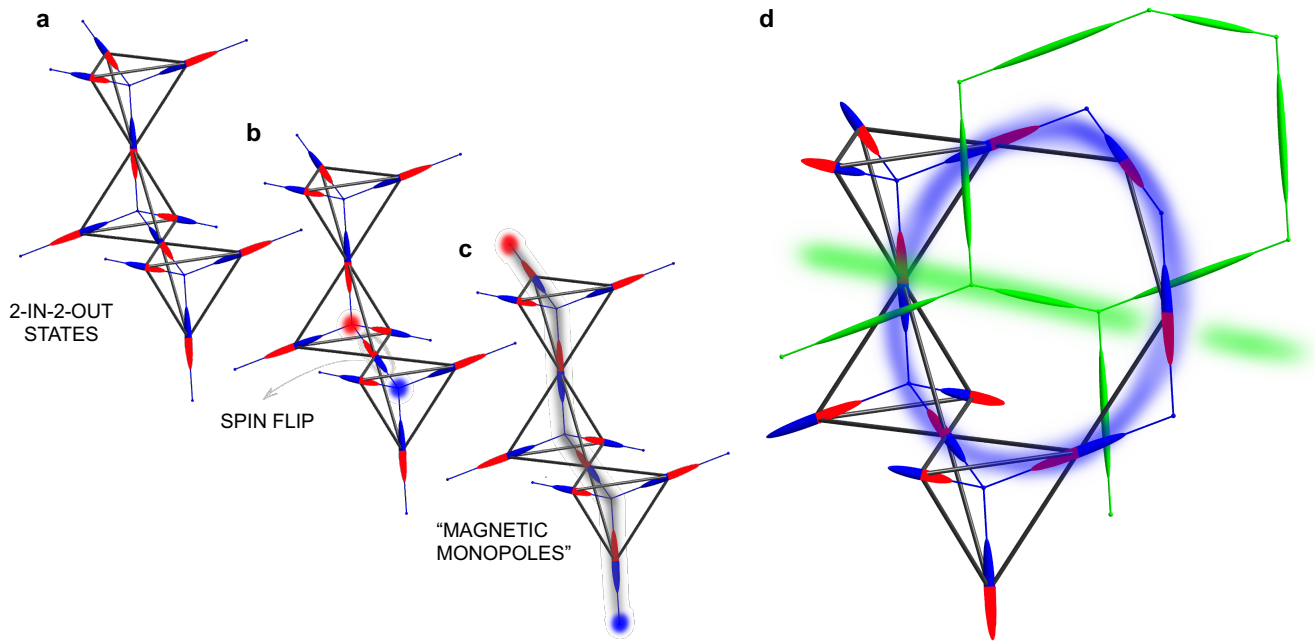


Figure 1 | Correlations and excitations in quantum spin ices. The ‘2-in-2-out’ ice configurations found in spin ices (a), as well as the creation (b) and propagation (c) of ‘magnetic monopole’ quasiparticles. The ellipses represent uniaxial magnetic moments, with blue and red poles, defining magnetic flux variables that live on a diamond lattice (blue lines). In $\text{Ce}_2\text{Sn}_2\text{O}_7$ the ice rule applies similarly on objects of a more complex magnetization density (magnetic octupoles)^{12,38–39}. In classical spin ice, thermal fluctuations create spin flips leading to fractional magnetic charges propagating through the sample (blue and red spheres). In a quantum spin ice (QSI)^{5–6}, the corresponding fractional gapped excitations (spinons) execute quantum coherent motion. The dominant tunneling process in QSI occurs on hexagonal plaquettes highlighted by the blue loop on panel d. This quantum dynamics is encoded by the fluctuation of electric flux variables living on a second diamond lattice (drawn in green) interpenetrating the first one. In this emergent quantum electrodynamics, transverse fluctuations of the dual gauge field are gapless ‘magnetic photon’ excitations^{5–6}.

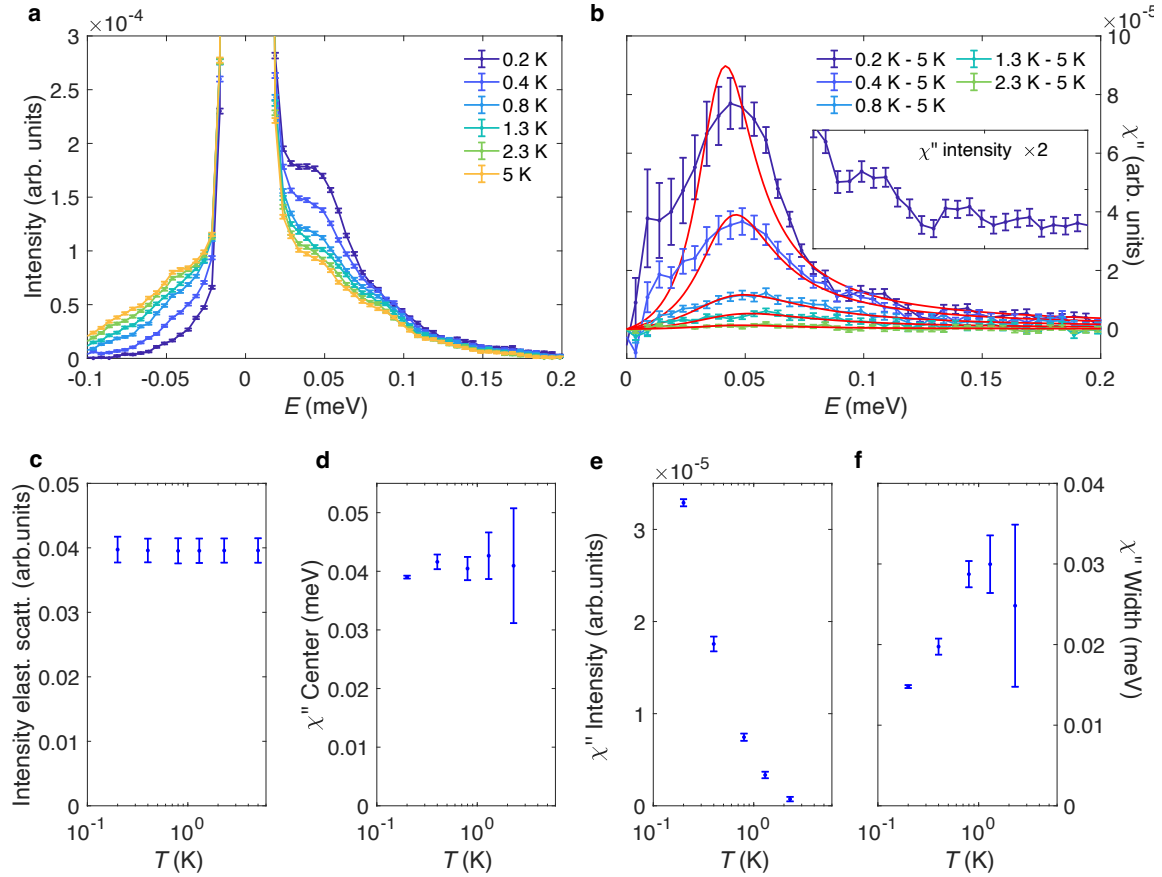


Figure 2 | Temperature evolution of spin excitations in $\text{Ce}_2\text{Sn}_2\text{O}_7$. **a**, Inelastic neutron scattering data measured at the time-of-flight spectrometer IN5 using an incident wavelength of 10 \AA , providing an energy resolution of $11 \mu\text{eV}$. The spectra were collected at various temperatures indicated in the plot, integrated on a range of momentum transfers $|\mathbf{Q}|$ from 0.3 to 1.1 \AA^{-1} and corrected for instrumental background, resulting in the experimental data points with error bars corresponding to ± 1 standard error. **b**, Imaginary part of the dynamic spin susceptibility $\chi''(E)$ (data points with error bars corresponding to ± 1 standard error) extracted from the data shown in panel **a**, as described in the main text. The red lines represent phenomenological Lorentzian fits of the data, allowing to numerically track the temperature dependence of the spin excitations. The fit function is defined as $\chi''(E) = \frac{S_f \gamma E}{(E-\delta)^2 + \gamma^2}$, with S_f a global scale factor, γ the Lorentzian width and δ its center. Panel **c** shows the temperature evolution of the scattering at the elastic line, with error bars corresponding to ± 1 standard error, indicating that the magnetic scattering in the accessible $|\mathbf{Q}|$ range is essentially inelastic. Panels **d**, **e** and **f** present the temperature dependence of the center, intensity and width of the Lorentzian fit to the $\chi''(E)$ data, respectively, with error bars corresponding to ± 1 standard error.

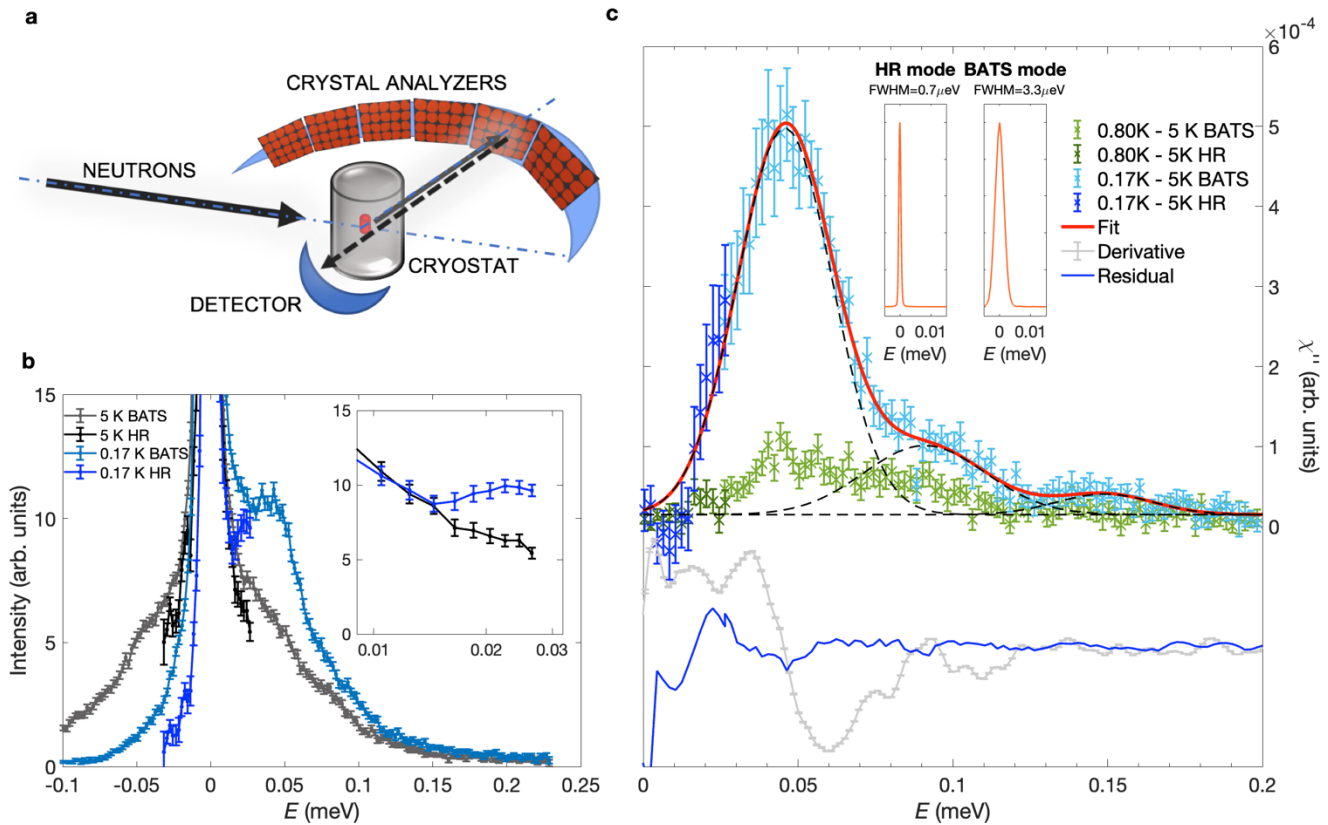


Figure 3 | High-resolution neutron spectroscopy of fractional excitations in $\text{Ce}_2\text{Sn}_2\text{O}_7$. **a**, Sketch of the neutron backscattering technique. Neutrons are first scattered by the sample towards crystal analyzers – a component that discriminates their energy with a very high resolution, and then backscattered towards a detector¹⁰. **b**, Comparison of the $\text{Ce}_2\text{Sn}_2\text{O}_7$ spectra collected at 0.17 K and 5 K using the IN16B instrument (Institut Laue–Langevin, Grenoble) in ‘backscattering and time-of-flight spectrometer’ (BATS)³⁴ and ‘high-resolution’ (HR)⁴⁸ modes. The spectra (data points with error bars corresponding to ± 1 standard error) were integrated on an identical range of momentum transfers $|\mathbf{Q}|$ (0.4 to 1.7 \AA^{-1}) and rescaled on the basis of their respective elastic line intensities, effectively correcting any discrepancies between the two configurations. The inset shows a zoom into the HR data, focusing on the threshold part of the spectra and showing the clear rise of the continuum on top of the remaining paramagnetic quasi-elastic signal. The latter is attributed to fluctuations of the dipole components of the pseudo-spin at finite temperatures. **c**, Superposition of the imaginary part of the dynamical spin susceptibility, $\chi''(E)$ (data points with error bars corresponding to ± 1 standard error), extracted from the continuation of HR (dark colored symbols) and BATS (light colored symbols) experiments at 0.17 K (blue shades) and 0.8 K (green shades). The continuous red line is a fit using a constant background and three Gaussian peaks individually shown as dashed black curves. The centers, intensities and widths are unconstrained, confirming the significance of each contribution to the spectrum. The continuous blue line and the grey points are the residual of the fit and the derivative of the experimental data, respectively, both shifted by -1.5 arbitrary units for clarity. The two insets in panel **c** show the energy resolution provided by each instrument configuration, on the same energy scale as the main panel.

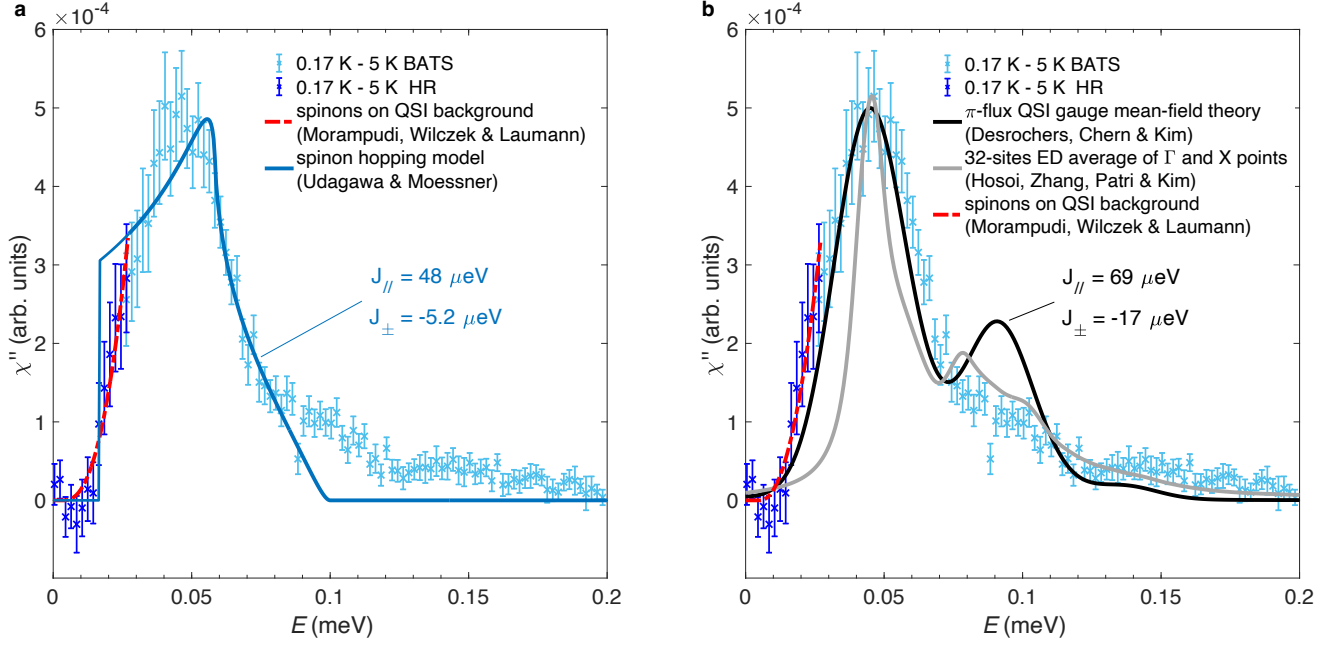


Figure 4 | Comparison of the dynamical spin susceptibility with models of spinon dynamics for the π -flux phase of quantum spin ice. In **a**, the continuous blue line is a fit of the combined HR and BATS data on their full energy window at 0.17 K, using the analytical model of Udagawa & Moessner for the quantum dynamics of spinons hopping on a lattice and considering a classical spin ice background¹³. Similarly, in **b**, we show the best fit using the gauge mean field theory of quantum spin ice revised by Desrochers, Chern & Kim¹⁵⁻¹⁶. In both these fits, the adjustment variables are exchange parameters $J_{||}$ and J_{\pm} whose fitted values are indicated in the respective panels, corresponding to $J_{\pm}/J_{||} = -0.1083$ (**a**) and $J_{\pm}/J_{||} = -0.2464$ (**b**). The fit using the gauge mean-field theory incorporates a peak broadening (standard deviation $\sigma = 11.2 \mu\text{eV}$). In panel **b**, we also compare the fit with available results of numerical calculations for $J_{\pm}/J_{||} = -0.1875$ using exact diagonalization on 32 sites (Hosoi, Zhang, Patri & Kim⁴⁴). The corresponding curve (solid grey line) is the average of results at the Γ and X points of the Brillouin zone after setting the energy scale of $J_{||}$ to the value determined from the fit of the gauge mean field theory. The red dashed lines in panels **a** and **b** use the analytical model of Morampudi, Wilczek & Laumann considering a QSI background, i.e., including photons, which effectively broadens the threshold for our experimental $|\mathbf{Q}|$ window due to the emission of Cerenkov radiation¹⁴. These QED effects are neglected in the other models, while the model of Morampudi *et al.* neglects the lattice and therefore can only be used to compare with data at the lower edge of the continuum. We used a numerical estimate for the fine-structure constant, $\alpha = 0.08$ (ref. 17), and other QED parameters obtained from the conversion of the exchange parameters $J_{||}$ and J_{\pm} deduced from the fits to either the spinon hopping model (blue line on panel **a**) or gauge mean field theory (black line on panel **b**) – see Methods. The red dashed line in panel **a** is a fit, whose only free parameter is the spinon gap $\Delta = 18 \mu\text{eV}$, while in panel **b** we impose the spinon gap $\Delta = 16.6 \mu\text{eV}$ which is the value predicted by the gauge mean-field theory for the exchange parameters obtained from the corresponding fit.

References

1. Balents, L. Spin liquids in frustrated magnets. *Nature* **464**, 199 (2010).
2. Savary, L. & Balents, L. Quantum spin liquids: a review. *Rep. Prog. Phys.* **80**, 016502 (2016).
3. Knolle, J. & Moessner, R. A Field Guide to Spin Liquids. *Annu. Rev. Condens. Matter Phys.* **10**, 451–472 (2019).
4. Broholm, C. *et al.* Quantum spin liquids. *Science* **367**, eaay0668 (2020).
5. Hermele, M., Fisher, M. P. A. & Balents, L. Pyrochlore photons: The $U(1)$ spin liquid in a $S = \frac{1}{2}$ three-dimensional frustrated magnet. *Phys. Rev. B* **69**, 064404 (2004).
6. Gingras, M. J. P. & McClarty, P. A. Quantum spin ice: a search for gapless quantum spin liquids in pyrochlore magnets. *Rep. Prog. Phys.* **77**, 056501 (2014).
7. Tennant, D. A., Perring, T. G., Cowley, R. A., & Nagler, S. E. Unbound spinons in the spin-1/2 antiferromagnetic chain KCuF_3 . *Phys. Rev. Lett.* **70** 4003–4006 (1993).
8. Lake, B., Tennant, D., Frost, C. & Nagler, S. E. Quantum criticality and universal scaling of a quantum antiferromagnet. *Nature Mater* **4**, 329–334 (2005).
9. Mourigal, M., Enderle, M., Klöpperpieper, A. *et al.* Fractional spinon excitations in the quantum Heisenberg antiferromagnetic chain. *Nature Phys* **9**, 435–441 (2013).
10. Gardner, J. S., Ehlers, G., Faraone, A. & Sakai, V. G. High-resolution neutron spectroscopy using backscattering and neutron spin-echo spectrometers in soft and hard condensed matter. *Nature Rev. Phys.* **2**, 103–116 (2020).
11. Sibille, R. *et al.* Candidate Quantum Spin Liquid in the Ce^{3+} Pyrochlore Stannate $\text{Ce}_2\text{Sn}_2\text{O}_7$. *Phys. Rev. Lett.* **115**, 097202 (2015).
12. Sibille, R. *et al.* A quantum liquid of magnetic octupoles on the pyrochlore lattice. *Nature Phys.* **16**, 546–552 (2020).
13. Udagawa, M. & Moessner, R. Spectrum of itinerant fractional excitations in quantum spin ice. *Phys. Rev. Lett.* **122**, 117201 (2019).
14. Morampudi, S. D., Wilczek, F. & Laumann, C. R. Spectroscopy of spinons in Coulomb quantum spin liquids. *Phys. Rev. Lett.* **124**, 097204 (2020).
15. Desrochers, F., Chern, L. E. & Kim, Y. B. Symmetry fractionalization in the gauge mean-field theory of quantum spin ice. *Phys. Rev. B* **107**, 064404 (2023).
16. Desrochers, F. & Kim, Y. B. Spectroscopic signatures of fractionalization in octupolar quantum spin ice. [arXiv:2301.05240](https://arxiv.org/abs/2301.05240)
17. Pace, S. D., Morampudi, S. C., Moessner, R. & Laumann, C. R. Emergent Fine Structure Constant of Quantum Spin Ice Is Large. *Phys. Rev. Lett.* **127**, 117205 (2021).
18. Wen, X-G. Topological Order: From Long-Range Entangled Quantum Matter to a Unified Origin of Light and Electrons. *ISRN Condensed Matter Physics* **2013**, 198710 (2013).
19. Levin, M. & Wen, X.-G. Colloquium: Photons and electrons as emergent phenomena. *Rev. Mod. Phys.* **77**, 871 (2005).
20. Eisenstein, J. P. & Stormer, H. L. The Fractional Quantum Hall Effect. *Science* **248**, 1510-1516 (1990).
21. Essin, A. M. & Hermele, M. Classifying fractionalization: Symmetry classification of gapped \mathbb{Z}_2 spin liquids in two dimensions. *Phys. Rev. B* **87**, 104406 (2013).
22. Essin, A. M. & Hermele, M. Spectroscopic signatures of crystal momentum fractionalization. *Phys. Rev. B* **90**, 121102 (2014).
23. Castelnovo, C., Moessner, R. & Sondhi, S. L. Spin Ice, Fractionalization, and Topological Order. *Annu. Rev. Condens. Matter Phys.* **3**, 35–55 (2012).

24. Ramirez, A. P., Hayashi, A., Cava, R. J., Siddharthan, R. & Shastri, B. S. Zero-point entropy in 'spin ice'. *Nature* **399**, 333–335 (1999).
25. Castelnovo, C., Moessner, R. & Sondhi, S. L. Magnetic monopoles in spin ice. *Nature* **451**, 42–45 (2008).
26. Fennell, T. *et al.* Magnetic Coulomb Phase in the Spin Ice $\text{Ho}_2\text{Ti}_2\text{O}_7$. *Science* **326**, 415 (2009).
27. Shannon, N., Sikora, O., Pollmann, K. & Fulde, P. Quantum Ice: A Quantum Monte Carlo Study. *Phys. Rev. Lett.* **108**, 067204 (2012).
28. Benton, O., Sikora, O. & Shannon, N. Seeing the light: Experimental signatures of emergent electromagnetism in a quantum spin ice. *Phys. Rev. B* **86**, 075154 (2012).
29. Kato, S. & Onoda, S. Numerical Evidence of Quantum Melting of Spin Ice: Quantum-to-Classical crossover. *Phys. Rev. Lett.* **115**, 077202 (2015).
30. Lee, S.B., Onoda, S. & Balents, L. Generic quantum spin ice. *Phys. Rev. B* **86**, 104412 (2012).
31. Chen, G. Spectral periodicity of the spinon continuum in quantum spin ice. *Phys. Rev. B* **96**, 85136 (2017).
32. Gaudet, J. *et al.* Quantum spin ice dynamics in the dipole-octupole pyrochlore magnet $\text{Ce}_2\text{Zr}_2\text{O}_7$. *Phys. Rev. Lett.* **122**, 187201 (2019).
33. Gao, B. *et al.* Experimental signatures of a three-dimensional quantum spin liquid in effective spin-1/2 $\text{Ce}_2\text{Zr}_2\text{O}_7$ pyrochlore. *Nature Phys.* **15**, 1052–1057 (2019).
34. Appel, M., Frick, B & Magerl, A. A flexible high speed pulse chopper system for an inverted neutron time-of-flight option on backscattering spectrometers. *Sci. Rep.* **8**, 13580 (2018).
35. Paddison, J. A. M. *et al.* Continuous excitations of the triangular-lattice quantum spin liquid YbMgGaO_4 . *Nature Phys.* **13**, 117–122 (2017).
36. Huang, C.-J., Deng, Y., Wan, Y. & Meng, Z.-Y. Dynamics of topological excitations in a model quantum spin ice. *Phys. Rev. Lett.* **120**, 167202 (2018).
37. Rau, J. G. & Gingras, M. J. P. Frustrated Quantum Rare-Earth Pyrochlores. *Annu. Rev. Condens. Matter Phys.* **10**, 357–386 (2019).
38. Huang, Y.-P., Chen, G. & Hermele, M. Quantum Spin Ices and Topological Phases from Dipolar-Octupolar Doublets on the Pyrochlore Lattice. *Phys. Rev. Lett.* **112**, 167203 (2014).
39. Li, Y.-D. & Chen, G. Symmetry enriched $U(1)$ topological orders for dipole-octupole doublets on a pyrochlore lattice. *Phys. Rev. B* **95**, 041106 (2017).
40. Benton, O., Jaubert, L. D. C., Singh, R. R. P., Oitmaa, J. & Shannon, N. Quantum Spin Ice with Frustrated Transverse Exchange: From a π -Flux Phase to a Nematic Quantum Spin Liquid. *Phys. Rev. Lett.* **121**, 067201 (2018).
41. Smith, E. M. *et al.* Case for a $U(1)_\pi$ Quantum Spin Liquid Ground State in the Dipole-Octupole Pyrochlore $\text{Ce}_2\text{Zr}_2\text{O}_7$. *Phys. Rev. X* **12**, 021015 (2012).
42. Bhardwaj, A., Zhang, S., Yan, H. *et al.* Sleuthing out exotic quantum spin liquidity in the pyrochlore magnet $\text{Ce}_2\text{Zr}_2\text{O}_7$. *npj Quantum Mater.* **7**, 51 (2022).
43. Savary, L. & Balents, L. Coulombic Quantum Liquids in Spin-1/2 Pyrochlores. *Phys. Rev. B* **108**, 037202 (2012).
44. Hosoi, M., Zhang, E. Z., Patri, A. S. & Kim, Y. B. Uncovering Footprints of Dipolar-Octupolar Quantum Spin Ice from Neutron Scattering Signatures. *Phys. Rev. Lett.* **129**, 097202 (2022).
45. Yahne, D. R. *et al.* Dipolar spin ice regime proximate to an all-in-all-out Néel ground state in the dipolar-octupolar pyrochlore $\text{Ce}_2\text{Sn}_2\text{O}_7$. [arXiv:2211.15140](https://arxiv.org/abs/2211.15140)
46. Porée, V. *et al.* Dipolar-octupolar correlations and hierarchy of exchange interactions in $\text{Ce}_2\text{Hf}_2\text{O}_7$. [arXiv:2304](https://arxiv.org/abs/2304).

Acknowledgements

This work is based on experiments performed at the Institut Laue–Langevin, France. We thank Xavier Tonon and the whole team for Advanced Neutron Environments for their dedicated work running the dilution refrigerators at the Institut Laue–Langevin. Tom Fennell is warmly acknowledged for his continuous support throughout this project and for a careful reading of the manuscript. We thank Nic Shannon for fruitful discussions. We acknowledge funding from the Swiss National Science Foundation (R.S. and V.P., Grant No. 200021_179150), the U.S. National Science Foundation Division of Materials Research under the award DMR-1917511 (H.Y. and A.H.N.), and the Natural Sciences and Engineering Research Council of Canada (F.D. and YB.K.).

Author contributions

Project and experiments were designed by R.S. Sample preparation and characterization were performed by R.S. and V.P. Neutron scattering experiments were carried out by V.P., E.L., S.P. and R.S. with O.J. and M.A. as local contacts. Experimental data were analysed by V.P., E.L., S.P. and R.S. Calculations were performed by H.Y., F.D., YB.K. and A.H.N. The paper was written by R.S. with feedback from all authors.

Competing financial interests

The authors declare no competing financial interests.

Methods

Sample preparation

The sample used during this work is a large polycrystalline sample of $\text{Ce}_2\text{Sn}_2\text{O}_7$, which was also used in previous studies^{11–12}. The solid-state synthesis product results from an oxido-reductive reaction where metallic tin is employed to reduce cerium to the trivalent state. The sample was thoroughly investigated using diffraction techniques as well as thermogravimetry, confirming the high purity of the sample and its stoichiometry $\text{Ce}_2\text{Sn}_2\text{O}_{7.00\pm 0.01}$, which indicates that all cerium ions are magnetic and experience the same crystal-electric field environment. Fits of neutron pair distribution function data further indicate the absence of disorder or local distortions of the crystal structure¹².

Neutron scattering experiments

The time-of-flight inelastic neutron scattering experiment was performed with the IN5 time-of-flight spectrometer at the Institut Laue–Langevin, Grenoble, France⁴⁷. The $\text{Ce}_2\text{Sn}_2\text{O}_7$ powder was pressed into pellets and inserted inside a copper can (10 mm diameter, filled on a height of ~5 cm), which was then sealed, pressurized using 10 bars of helium gas at room temperature, and mounted below the mixing chamber of a dilution refrigerator. The helium overpressure was required in order to maximize cooling efficiency. An incident wavelength of 10 Å was used, providing an energy resolution of about 11 μeV at the elastic line. The cooling of the sample was monitored by following the evolution of the inelastic contribution to the signal. The temperature of the sample was estimated by fitting the spectrum using a phenomenological background function, a Gaussian centered at zero energy transfer and two gapped Lorentzian multiplied by $1/(1 - \exp(-\frac{E}{k_B T}))$ to account for temperature effects. The datasets were recorded in such a way to obtain similar statistics at each temperature. Calibration scans (vanadium

and empty copper can) were used to properly reduce the data using Mantid⁴⁸ routines, resulting in six pre-processed datafiles containing the $\|\vec{Q}\|$ -integrated spectra ($0.3 \text{ \AA}^{-1} < \|\vec{Q}\| < 1.1 \text{ \AA}^{-1}$).

Neutron backscattering spectroscopy was performed on IN16B at the Institut Laue-Langevin^{34,49}. The sample and sample preparation were identical to the IN5 experiment described above. In a first step, we used the BATS mode available at IN16B (ref. 34) in order to cover the full bandwidth of excitations in $\text{Ce}_2\text{Sn}_2\text{O}_7$. Two instrument configurations, denoted as Ir4 and Ir6, were used and correspond to low repetition rates with 8° and 11° slits in the pulse choppers, providing a resolution of 4 \mu eV and 6 \mu eV respectively. The Ir6 allowed to efficiently measure spectra at intermediate temperatures, benefiting from a more intense beam at the expense of a slightly coarser resolution with respect to Ir4. The thermalization of the sample was monitored as described for the IN5 experiment. Spectra were recorded at 0.17 K, 0.8 K and 5 K using both Ir4 and Ir6, with additional measurements at 0.4 K and 1.2 K with the Ir6 set-up. Data for a vanadium standard, empty copper can and empty dilution were also recorded and used in the reduction routines using Mantid⁴⁸. The spectra were integrated over the same $\|\vec{Q}\|$ window ranging from 0.4 \AA^{-1} to 1.7 \AA^{-1} . The resulting data can be seen in Fig. 3b and Fig. S1a, for Ir4 and Ir6 respectively. The imaginary part of the dynamical spin susceptibility was computed following the same method as described above and the results are shown in Fig. 3c (as well as Fig. 4a and 4b) and Fig. S1b, for Ir4 and Ir6, respectively.

A second experiment was carried out on IN16B, in order to better investigate the lower part of the energy spectrum. The High-Resolution (HR) mode of the instrument was used, which has a lower flux compared to the previously mentioned BATS mode, and a resolution at the elastic line of about 0.7 \mu eV . We have used a specialized high signal-to-noise ratio setup of the IN16B spectrometer previously reported⁴⁹. The same powder sample was again used but this time was loaded in a copper can with annular geometry (outer 15 mm, inner 10 mm). The reason for such a choice was the reduction of the neutron absorption by the sample, which in this geometry, plays a more important role. The sample was cooled down to an estimated base temperature of approximately 0.17 K. Data were recorded at three different temperatures, 0.17 K, 0.8 K and 5 K with similar statistics, allowing to track the signal's behavior and a direct comparison with previous experiments. The data were reduced via Mantid⁴⁸ routines, using carefully measured calibration scans (vanadium sheets, empty annular copper can and empty dilution refrigerator). The resulting spectra were then integrated over a $\|\vec{Q}\|$ window ranging from 0.4 \AA^{-1} to 1.7 \AA^{-1} . The final spectra can be seen in Fig. 3b. The imaginary part of the dynamical spin susceptibility was computed following the same method as described above and is plotted in Fig. 3c as well as in Fig. 4a and 4b. In order to get a meaningful comparison of the BATS and HR data, the Ir4 HR spectra were subject to a minor rescaling, based on the relative intensities at the elastic line, thus compensating for any discrepancies between the two instrument modes.

Fitting of the experimental data to model calculations

We consider a Hamiltonian where the transverse exchange parameter J_\pm introduces quantum fluctuations to a classical spin ice manifold obtained from a dominant nearest-neighbor ferromagnetic interaction J_\parallel :

$\mathcal{H}_{QSI} = \mathcal{H}_{CSI} + \mathcal{H}_{transverse} = \sum_{(i,j)} J_\parallel S_i^y S_j^y - J_\pm (S_i^+ S_j^- + S_i^- S_j^+)$. Here S^y corresponds to the octupolar component of the 'dipole-octupole' pseudo-spin³⁷⁻³⁹, stabilizing an octupole ice manifold in $\text{Ce}_2\text{Sn}_2\text{O}_7$ (ref. 12).

We first used the results of Udagawa and Moessner¹³ to compare with our data. They found that the two-spinon density of state (DOS) can be well approximated by the following exact result $\rho_{\text{HC}}^{(2)}(\omega) = \int d\epsilon \rho_{\text{HC}}^{(1)}(\omega - \epsilon) \times \rho_{\text{HC}}^{(1)}(\epsilon)$ where $\rho_{\text{HC}}^{(1)}(\epsilon) = \frac{3}{2\pi} \frac{1}{6-\epsilon} \sqrt{\frac{5-\epsilon}{3+\epsilon}}$ is the single spinon DOS with $\epsilon = (\omega - J_{\parallel})$ in arbitrary units. We compare $\rho_{\text{HC}}^{(2)}(\omega)$ directly with our experimental data. We vary an overall scale factor and the parameters J_{\parallel} and J_{\pm} (after converting them into the meV units), to minimize the least-mean square difference between the theory and all the experimental data (BATS Ir4, BATS Ir6 and HR): $C_1 = \sum_{\omega \text{ in exp.}} (I_{\text{exp}}(\omega) - a \times \rho_{\text{HC}}^{(2)}(\omega))^2$. Here, the parameters J_{\parallel} , J_{\pm} are inside the definition of $\rho_{\text{HC}}^{(2)}(\omega)$ but we did not write them out explicitly to lighten the notation. J_{\parallel} is used in defining $\epsilon = \omega - J_{\parallel}$ in the single spinon DOS, and J_{\pm} is determined when converting the unit of ϵ to meV. Here, the parameter a is the overall scaling factor that we also fit. We found that the square sum is minimized by the following parameters $J_{\parallel} = 48 \mu\text{eV}$, $J_{\pm} = -5.2 \mu\text{eV}$ and $J_{\text{ring}} \equiv \frac{12J_{\pm}^3}{J_{\parallel}^2} = 0.73 \mu\text{eV}$.

Second, we fit the experimental $\chi''(E)$ data to the gauge mean-field theory results of Desrochers, Chern and Kim¹⁵⁻¹⁶. We used the positions identified from the data as starting values for the centers of the three peaks expected for the π -flux phase of quantum spin ice. The goodness of fit measures are defined as

$$\chi_{\text{Direct}}^2 = \sum_n \frac{(I^{\text{Exp.}}(E_n) - I^{\text{Theo.}}(E_n))^2}{(\Delta I^{\text{Exp.}}(E_n))^2}$$

and

$$\chi_{\text{Peak}}^2 = \sqrt{\sum_{i=1}^3 (E_i^{\text{Theo.}} - E_i^{\text{Exp.}})^2 / E_i^{\text{Exp.}}}.$$

We normalize both χ_{Direct}^2 and χ_{Peak}^2 before taking the weighted sum. The final goodness of fit is $\chi^2 = \alpha \chi_{\text{Direct}}^2 + (1 - \alpha) \chi_{\text{Peak}}^2$ with $\alpha = 0.6$. We found that χ^2 is minimized using $J_{\parallel} = 69 \mu\text{eV}$, $J_{\pm} = -17 \mu\text{eV}$ and $J_{\text{ring}} \equiv \frac{12J_{\pm}^3}{J_{\parallel}^2} = 12.4 \mu\text{eV}$.

Finally, we used the above extracted exchange parameters from both the analytical model of Udagawa and Moessner¹³ and the extended gauge mean-field theory of Desrochers, Chern and Kim¹⁵⁻¹⁶, and applied these to the analytical model of Morampudi, Wilczek & Laumann¹⁴, which determined neutron scattering as

$$S(q, \omega, \Delta) = \frac{m^{3/2} \sqrt{2\pi R}}{1 - \exp\left(-\sqrt{\frac{2\pi R}{\omega - 2\Delta - q^2/4m}}\right)} \theta(\omega - 2\Delta - q^2/4m), \text{ where } R = \frac{1}{4} m c^2 \alpha^2 \left(1 - \frac{q^2}{4m^2 c^2}\right)^2.$$

Most parameters in this model are determined by the spin exchange parameters: the loop flipping term coefficient $g = 12 \frac{J_{\pm}^3}{J_{\parallel}^2}$, the spinon mass $m = \frac{1}{4J_{\pm} a_0^2}$, and the speed of light $c = \xi g a_0$. In addition, there are three constants independent of the value of J_{\parallel}, J_{\pm} , which are either known experimentally – the lattice constant $a_0 = 10.6 \times 10^{-10} \text{ m}$, or taken from numerical estimates¹⁷ – the emergent fine-structure constant $\alpha = 0.08$ and the O(1) constant $\xi = 0.51$. Therefore, a fit to experimental data using this QED model has only two free parameters. The first free parameter is the overall scale of the DOS, while the second one is the spinon gap Δ . Although Morampudi *et al.*¹⁴ take the gap to be $\Delta \sim J_{\parallel}/2 - 12J_{\pm}$, this value turns out to be negative from our

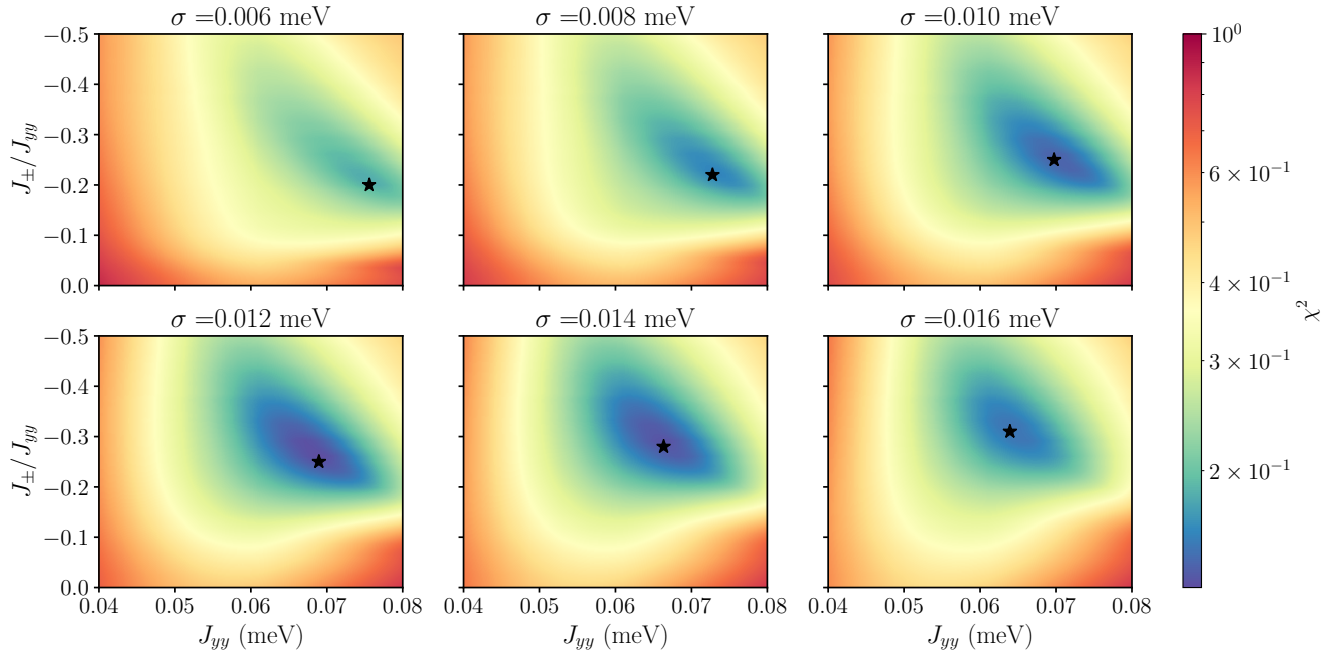
fitting result. We hence take Δ to be a free parameter when fitting the experimental neutron intensity to the theory. Since the work of Morampudi *et al.*¹⁴ is applicable in the long wavelength limit and does not consider the short wavelength effects of the pyrochlore lattice, it can only be used to compare with the low-energy end of the neutron scattering. In order to compare the model with the experimental data, we integrated over q to obtain the (local) density of states distribution $\tilde{S}(\omega, \Delta) = \int dq S(q, \omega, \Delta)$ and minimized the following quantity: $C_2 = \sum_{\omega \text{ in exp.}} (I_{\text{exp}}(\omega) - a \times \tilde{S}(\omega, \Delta))^2$. Here, a is the overall scaling factor and we use the low-energy HR dataset, which covers energy transfers up to 26.5 μeV . The best fit we found results in $\Delta = 18 \mu\text{eV}$ using the exchange parameters deduced from the analytical model of Udagawa and Moessner¹³. In order to calculate the low-energy response using the exchange parameters deduced from the extended gauge mean-field theory of Desrochers, Chern and Kim¹⁵⁻¹⁶, we have used the spinon gap value predicted by the same theory, $\Delta = 16.6 \mu\text{eV}$.

Data availability

The data that support the plots within this paper and other findings of this study are available from the corresponding authors upon reasonable request. The datasets for the time-of-flight neutron spectroscopy experiments on IN5 and for the backscattering neutron spectroscopy experiments on IN16B are available from the Institute Laue-Langevin data portal⁵⁰⁻⁵².

References (methods)

47. Ollivier, J. & Mutka, H. IN5 cold neutron time-of-flight spectrometer, prepared to tackle single crystal spectroscopy. *J. Phys. Soc. Jpn* **80**, SB003 (2011).
48. Arnold O. *et al.* Mantid—Data analysis and visualization package for neutron scattering and μSR experiments, *Nucl. Instrum. Methods Phys. Res. A* **764**, 156–166 (2014).
49. Appel, M. & Frick, B. Note: One order of magnitude better signal-to-noise ratio for neutron backscattering. *Rev. Sci. Instrum.* **88**, 036105 (2017).
50. Sibille, R. *et al.* (2020). Spin excitations of a quantum liquid of octupoles. Institut Laue-Langevin (ILL) [doi:10.5291/ILL-DATA.4-05-770](https://doi.org/10.5291/ILL-DATA.4-05-770)
51. Sibille, R. *et al.* (2021). Threshold effect and the continuum of spin excitations in the octupolar quantum spin ice $\text{Ce}_2\text{Sn}_2\text{O}_7$. Institut Laue-Langevin (ILL) [doi:10.5291/ILL-DATA.4-05-771](https://doi.org/10.5291/ILL-DATA.4-05-771)
52. Sibille, R. *et al.* (2021). Threshold effect and the continuum of spin excitations in the octupolar quantum spin ice $\text{Ce}_2\text{Sn}_2\text{O}_7$ – continuation. Institut Laue-Langevin (ILL) [doi:10.5291/ILL-DATA.DIR-249](https://doi.org/10.5291/ILL-DATA.DIR-249)



Extended data Fig. 1 | Goodness of fit for the adjustment of the exchange parameters of the gauge mean field theory to the $\chi''(E)$ data. The color maps show the goodness of fit defined in the Methods section, as a function of the dominant and transverse exchange parameters, for different values of the phenomenological peak broadening σ (standard deviation). Here, J_{yy} is an octupolar exchange interaction designating the dominant nearest-neighbor interaction J_{\parallel} . The fitting procedure is described in the Methods section and the final fit is presented in Fig. 4b (black curve).